Ultramicroscopy 168 (2016) 46–52

Contents lists available at ScienceDirect

Ultramicroscopy

journal homepage: www.elsevier.com/locate/ultramic

Oxygen octahedra picker: A software tool to extract quantitative information from STEM images

Yi Wang *, Ute Salzberger, Wilfried Sigle, Y. Eren Suyolcu, Peter A. van Aken

Stuttgart Center for Electron Microscopy, Max Planck Institute for Solid State Research, Heisenbergstr. 1, 70569 Stuttgart, Germany

ARTICLE INFO

Article history:
Received 22 January 2016
Received in revised form
21 April 2016
Accepted 6 June 2016
Available online 15 June 2016

Keywords:
Quantitative STEM image analysis
BO_6 octahedral distortion
Annular bright-field (ABF) imaging
Atomic column locating

ABSTRACT

In perovskite oxide based materials and hetero-structures there are often strong correlations between oxygen octahedral distortions and functionality. Thus, atomistic understanding of the octahedral distortion, which requires accurate measurements of atomic column positions, will greatly help to engineer their properties. Here, we report the development of a software tool to extract quantitative information of the lattice and of BO_6 octahedral distortions from STEM images. Center-of-mass and 2D Gaussian fitting methods are implemented to locate positions of individual atom columns. The precision of atomic column distance measurements is evaluated on both simulated and experimental images. The application of the software tool is demonstrated using practical examples.

1. Introduction

The multifaceted magnetic, electrical, and structural functionalities of perovskite oxides are underpinned by the distortions of the crystal lattice [1]. These distortions include the displacement of cations, deformation of oxygen octahedra (BO_6, where B is a transition metal atom), and collective tilts of the octahedral network. Controlling and engineering these distortions in the constituent oxides are crucial in designing and fabricating heterostructures with novel functional properties that are absent in the bulk form. Atomistic understanding of these distortions and elucidation of their influence on the final properties requires imaging and measuring of atomic positions of both cations and oxygen. Atomic resolution (scanning) transmission electron microscopy (TEM/STEM) provides an essential tool to image these atomic structures of materials, and helps us to understand the structure – property relationship. With the application of spherical aberration (C_s) correctors, sub-Angstrom atomic resolution is nowadays regularly achievable in both TEM and STEM [2]. Although imaging atomic resolution of heavy elements has been possible since the 1980s, light-element STEM imaging has become possible only recently using the annular bright-field (ABF) imaging technique [3], enabling imaging of, e.g., oxygen [3–5], nitrogen [5], lithium [6], and hydrogen [7]. The application of the ABF imaging technique in perovskite oxides has become increasingly popular, as it enables simultaneous imaging of heavy and light elements and allows for simultaneous acquisition of other signals, for example electrons scattered to large angles (high-angle annular dark-field (HAADF), also called *Z*-contrast imaging), characteristic X-rays (energy-dispersive X-ray spectroscopy (EDXS)), and electron energy loss (EELS) [4]. Quantitative analysis of these atomic resolution images often requires the extraction of atomic column positions and intensities, and measurement of atomic-column distances at the unit-cell level and beyond. Such quantitative analysis of atomic column information helps us gain new insight into materials behavior by characterizing ferroelectricity [8,9], composition [10–13], octahedral tilting [14,15], and strain [16]. Despite the great success of atomic resolution image analysis and application in addressing materials problems, there are rare resources about methods for indexing atomic column positions in atomic resolution images, especially for the case of ABF images, as well as for the measurement accuracy. Therefore, there is great need for a robust and easy-to-use tool to identify and measure both light and heavy atom columns in ABF and HAADF images and to enable quantification of both crystal lattice and BO_6 octahedral distortions.

Here, we report the development of a software tool, which we call oxygen octahedra picker (O–O Picker), for robust mapping of atomic column positions from the HAADF and ABF images.

2. Algorithm

2.1. Algorithm for atomic column locating

Two methods have been implemented in this software for locating individual atomic columns, the center-of-mass and two

* Corresponding author.
E-mail address: y.wang@fkf.mpg.de (Y. Wang).

http://dx.doi.org/10.1016/j.ultramic.2016.06.001

dimensional (2D) Gaussian fitting, both giving sub-pixel precision [17].

In the center-of-mass method (also referred to as the moment method or the centroid method), the peak center of an atomic column is given by

$$C_x = \frac{\sum_i \sum_j (x_i \cdot I_{ij})}{\sum_i \sum_j I_{ij}} \text{ and } C_y = \frac{\sum_i \sum_j (y_i \cdot I_{ij})}{\sum_i \sum_j I_{ij}},$$

where x_i and y_j are the positions along the x and y axes, and I_{ij} is the image intensity of pixel (i, j) [17]. The summation is performed across an area covering the whole atomic column. Because of the simplicity and computational speed, it is one of the most widely used methods when analyzing large quantities of data [18].

For the 2D Gaussian fitting method, the intensity of each atomic column was fitted to a 2D Gaussian function plus a constant [17,19]

$$I(x, y) = I_0 + A^* \exp\left\{\left(-\frac{1}{2}\left[\left(\frac{x - x_0}{x_w}\right)^2 + \left(\frac{y - y_0}{y_w}\right)^2\right]\right)\right\}.$$

The fit parameters are the background I_0, the Gaussian amplitude A, the atomic column widths x_w, and y_w, and the atomic column position x_0 and y_0. Each atomic column was fitted to an optimized 2D Gaussian function.

The center-of-mass method is set as the default routine, since it is much faster than 2D Gaussian fitting. In case the 2D Gaussian fitting method is active the program will take the results of the center-of-mass method as the initial input for 2D Gaussian fitting iteration.

2.2. Steps of analysis

The software tool, written in Digital Micrograph (DM, Gatan Inc) scripting language [20], is divided into several sequential steps, which are summarized in the flow chart in Fig. 1(a). The user interface of this script is shown in Fig. 1(b). If HAADF (or annular dark-field (ADF)) and ABF images were simultaneously acquired, one can use the HAADF image to locate the B atomic column positions. However, using the input of HAADF (or ADF) image is optional and determining B-atomic-column positions can also be performed directly on the ABF image. The script "B atom navigator" (Fig. 1b) is used to locate the B site atomic columns. One has to set proper atomic radii (value in pixel, the pixel size of the "atomic radius" should be large enough to cover the atomic column, but it should not reach neighboring atomic columns), and number of B atoms to search along the vertical direction. After pressing the "Get B atom" button B atomic columns will be found and the location of the B atom column will be marked by circles on the HAADF image. Once the B atomic columns are found, one has to mark four O atoms surrounding a B atom by using the annotation tool (i.e. the HREM mouse tool [21]) in the ABF image. After pressing "Scan Annotation" to select the target ABF image, one has to check whether the four corner O atomic columns are marked properly, and to input the proper atomic radii (value in pixel) for the O atomic columns. By clicking the button "Get O peak", the oxygen atomic positions on the ABF image will be detected by an iterative process locating positions of atomic columns by either center-of-mass or 2D Gaussian fitting. Results of the atomic column locations are marked by circles in a copy of the original ABF image, from which one can visually check whether the initial inputs were properly selected. Once the initial octahedron is located properly, click the "Get more" button, the program will then take the located B atomic column position as a guide to detect all the octahedra on the image. The final results provided by the software are the

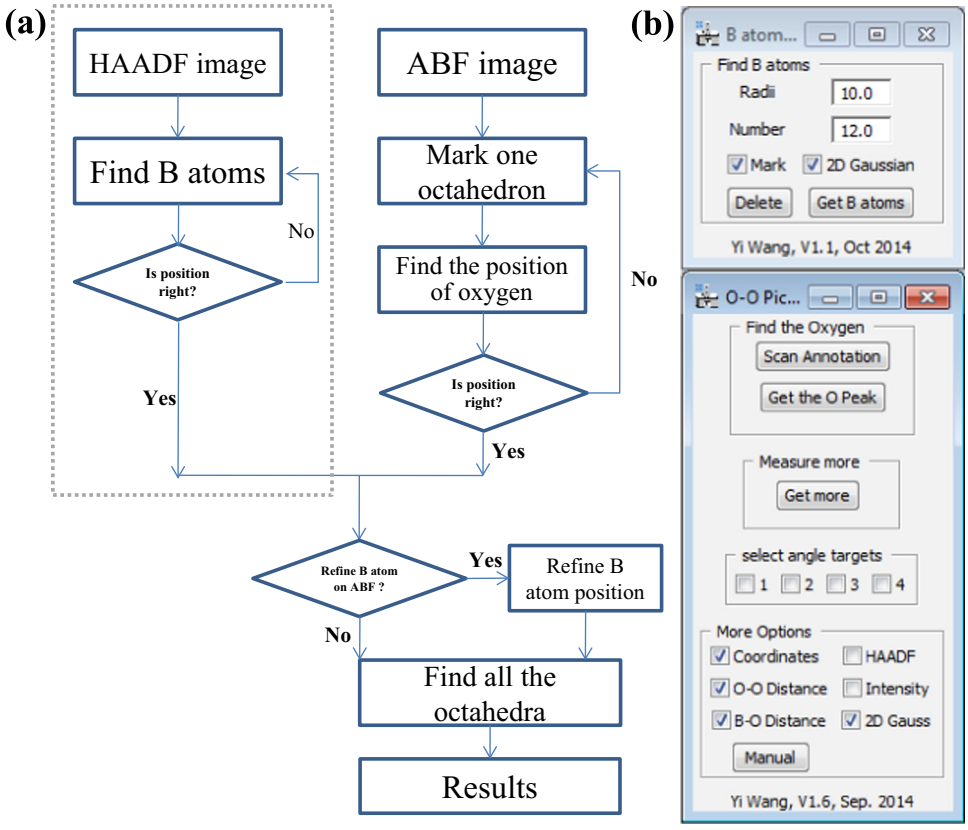

Fig. 1. (a) Flow chart of the script, starting with the image(s) and ending in the results. (b) The user interface of the scripts, B atom navigator (top) and O–O picker (bottom).

coordinates of detected atomic columns, the atomic column intensities, the distances between the atomic columns, and the angles between selected atomic columns, based on the selection of the user. The outputs are printed in the results window as text and stored as a tags file in the copied ABF image for advanced users. By selecting the "HAADF" option, one can use this program to also analyze the HAADF image in the sample procedure. When selecting the ABF image for processing, if both raw ABF image and de-noised ABF image are selected, the de-noised image will be used as a starting image for a rough detection of atom column positions, and final fitting of positions by the center-of-mass or 2D Gaussians are performed on the original raw image [22]. The software (plug-in for DM) is available by request to the authors.

3. Experimental section

As examples to illustrate the result of the O–O picker program, $SrTiO_3$ bulk material and La_2CuO_4 (LCO) thin film grown on $LaSrAlO_4$ (LSAO) substrate were selected. The epitaxial deposition of La_2CuO_4 by atomic layer-by-layer oxide molecular beam epitaxy has been described by Baiutti [23]. TEM specimens were prepared by a standard procedure which included mechanical grinding, tripod polishing, and argon ion beam milling in a stage cooled with liquid nitrogen. Before STEM experiments, samples were plasma-cleaned by a Fischione plasma cleaner in a 75% argon – 25% oxygen mixture for 4 min to eliminate hydrocarbon surface contamination. STEM investigations were performed using a JEOL JEM-ARM 200F scanning transmission electron microscope equipped with a cold field emission electron source, a DCOR probe corrector (CEOS GmbH), a 100 mm^2 JEOL Centurio EDX detector, and a Gatan GIF Quantum ERS electron energy-loss spectrometer. The microscope was operated at 200 kV with a semi-convergence angle of 20.4 mrad, giving rise to a probe size of 0.8 Å. 75–309 mrad and 11–24 mrad collection angles were used to simultaneously obtain the HAADF and ABF images, respectively. The fast scan direction during the STEM experiments is parallel to the horizontal axis of the presented images. In order to improve the signal-to-noise ratio (SNR) and to minimize the image distortion of HAADF and ABF images, 7 frames were acquired with a short dwell time (2 μs per pixel). The frame series was aligned by a Gatan image alignment plug-in in Digital Micrograph. The diagnosis of the sample drift between the frames was performed on the HAADF and the removal of the drift parameters were applied to both HAADF and ABF images. The aligned frames were then superimposed. The STEM images were de-noised by the multivariate weighted principal component analysis (PCA) routine (MSA Plugin in Digital Micrograph) developed by M. Watanabe [24]. STEM images were simulated using the multi-slice method implemented in the QSTEM image simulation software [25]. The optical parameters used for the simulation were the same as the experimentally used values. The thickness of supercells used in the STEM image simulation was 15 nm.

4. Method accuracy and precision

To evaluate the accuracy of the software and how the noise level influences the oxygen position detection, we tested this software tool on simulated ABF image of $SrTiO_3$ with different SNRs. Fig. 2(a) shows the overlay of simulated HAADF (green) and ABF (red) images, where O atomic columns are clearly resolved as dark dots on red background, while Ti and Sr atomic columns are resolved as gray-green and bright-green dots, respectively. Then,

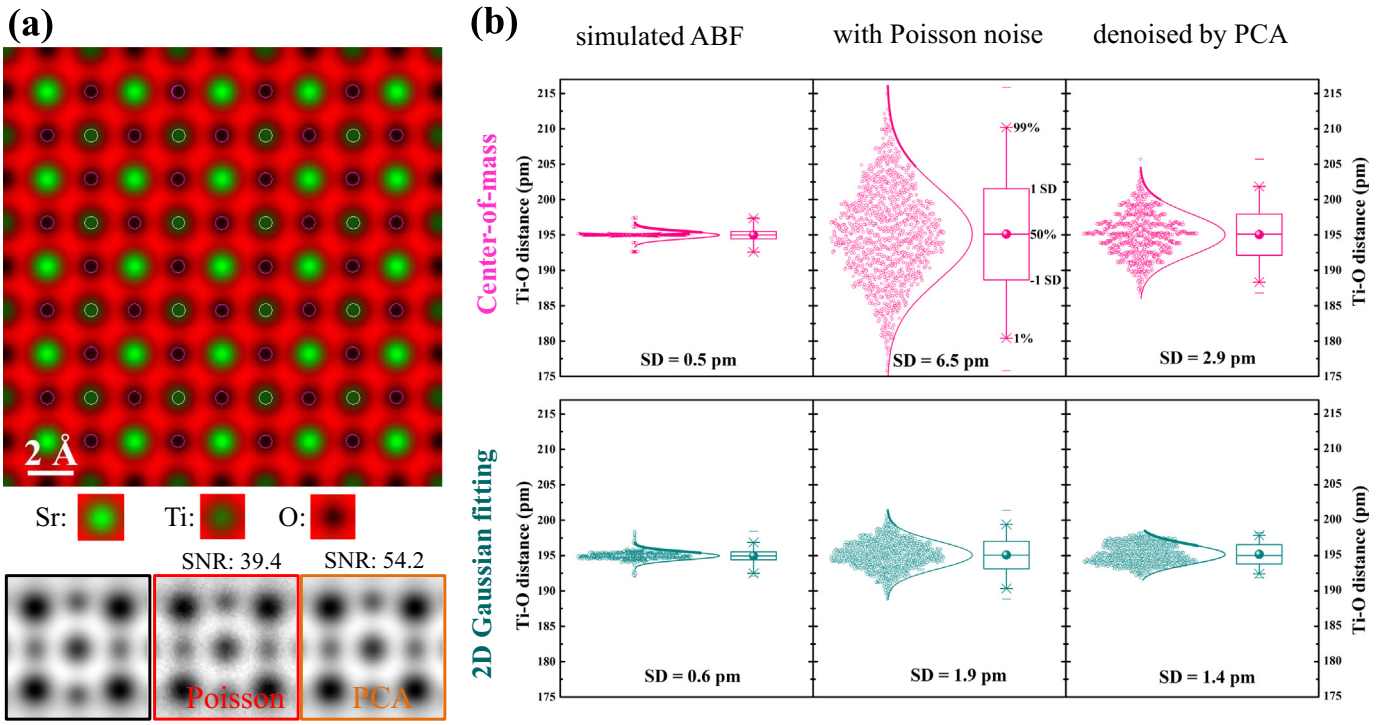

Fig. 2. (a) Selected area of simulated HAADF and ABF image of $SrTiO_3$. The atomic column detection accuracy is estimated on a simulated image, an image with Poisson noise, and an image de-noised by PCA, respectively. (b) Box-and-whisker plot of the measured Ti–O atomic column distances from simulated ABF images with different SNRs. The statistics are based on 324 TiO_6 octahedra (18 u.c. × 18 u.c.) measurements. The pink color shows the results using center-of-mass method, and the turquoise color shows the results using 2D Gaussian fitting. In each plot, the left panel shows the distribution of the raw data (the ordinate shows the measured distances, the width of scattering represents the relative frequency count) and a normal population curve; the right panel shows the summary of the statistics, the middle line in the box represents the median, the solid sphere is the mean, the box defines the standard deviation, and the whisker defines the 1%-99% range of the raw data. (For interpretation of the references to color in this figure legend, the reader is referred to the web version of this article.)

Poisson noise was added to the simulated HAADF and ABF images and PCA was applied to de-noise the images. The bottom panel of Fig. 2(a) shows a selected area of these ABF images, where a unit cell of $SrTiO_3$ is presented. The SNR was calculated based on the method reported by Gonzalez et al. [26]. We performed oxygen atomic column mapping and measured the Ti and O atomic column distances directly on the above mentioned three types of images. Following Bals et al. [27], we define the image measurement precision as the standard deviation of the measured distances. Fig. 2(b) shows the distribution of measured distances and a summary of the statistics illustrating accuracy and precision of the oxygen octahedral location for the three different image noise levels. The statistics were based on a large image covering more than 324 oxygen octahedra (18 u.c. × 18 u.c.). In all the cases, the measured mean Ti–O distance is 195 pm, equal to the theoretical value, highlighting the high measurement accuracy for both center of mass and 2D Gaussian fitting methods. For the simulated image without Poisson noise, the center-of-mass and 2D Gaussian fitting give precisions of 0.53 pm and 0.82 pm, respectively, i.e. both show sub-pm precision. In the presence of Poisson (shot) noise, which is the dominant source of the noise in STEM imaging [28,29], 2D Gaussian fitting is almost 3 times more precise than the center-of-mass method. On the image de-noised by PCA (with 15 components) center-of-mass and 2D Gaussian fitting show precisions of 2.92 pm and 1.38 pm, respectively. The presence of Poisson noise degrades the measurements precision of both center-of-mass and 2D Gaussian fitting methods, whereas the center-of-mass method is more sensitive to Poisson noise.

A similar measurement was performed on experimental images using frame serial acquisition, post-image alignment, and PCA filtering. Fig. 3 shows the atomically resolved ABF (a) and HAADF (b) images. Raw STEM images before and after alignment are presented in the Supplementary movies 1–4. As can be seen from the movies, sample drift is present during the frame serial acquisition and the measured sample drift rate is 0.08 nm/s. The measurement accuracy and precision test is performed on both ABF and HAADF images by measuring the Ti–Sr and Ti–O atomic column distances, respectively. Again we can see from the summary of the statistics, that both methods give very high accuracy and the measured Ti–Sr and Ti–O distances are equal to the theoretical values (276.125 pm and 195.25 pm, respectively). To quantify the measurement precision we first perform the analysis directly on the raw aligned STEM images. As can be seen from Fig. 3(c) and (d), the center-of-mass method shows precisions of 5.1 pm and 10.0 pm for HAADF and ABF images, respectively. With 2D Gaussian fitting refinement, the measurement precision improves to 3.1 pm and 5.0 pm for HAADF and ABF images, as illustrated in Fig. 3(e) and (f), respectively. For comparison, a more sophisticated method, as demonstrated by van Aert et al. [22], is used to improve the measurement precision. We take the de-noised image as an improved start for roughly detecting the atomic column position and perform the final fitting of the atomic column on the raw aligned STEM images. As can be seen from Fig. 3(h) and (i), for the center-of-mass method the improvement in measurement precision is remarkable and we achieve 3.1 pm and 5.4 pm for HAADF and ABF images, respectively. With 2D Gaussian fitting, the measurement precision further improves to 3.0 pm and 4.0 pm for HAADF and ABF images, respectively. In all the cases, better precision can be achieved for both atomic-column detecting methods on HAADF images, since the peak feature of heavy atomic columns in the HAADF imaging mode is more pronounced than of the O atomic columns in ABF images. To further improve the measurement precision, i.e. to achieve sub-pm precision, one may need a more stable experimental environment, to use more frames for averaging for better SNR, and to use more advanced image alignment algorithms, i.e. non-rigid registration techniques [19,30], which corrects both image drift and local scanning-distortions.

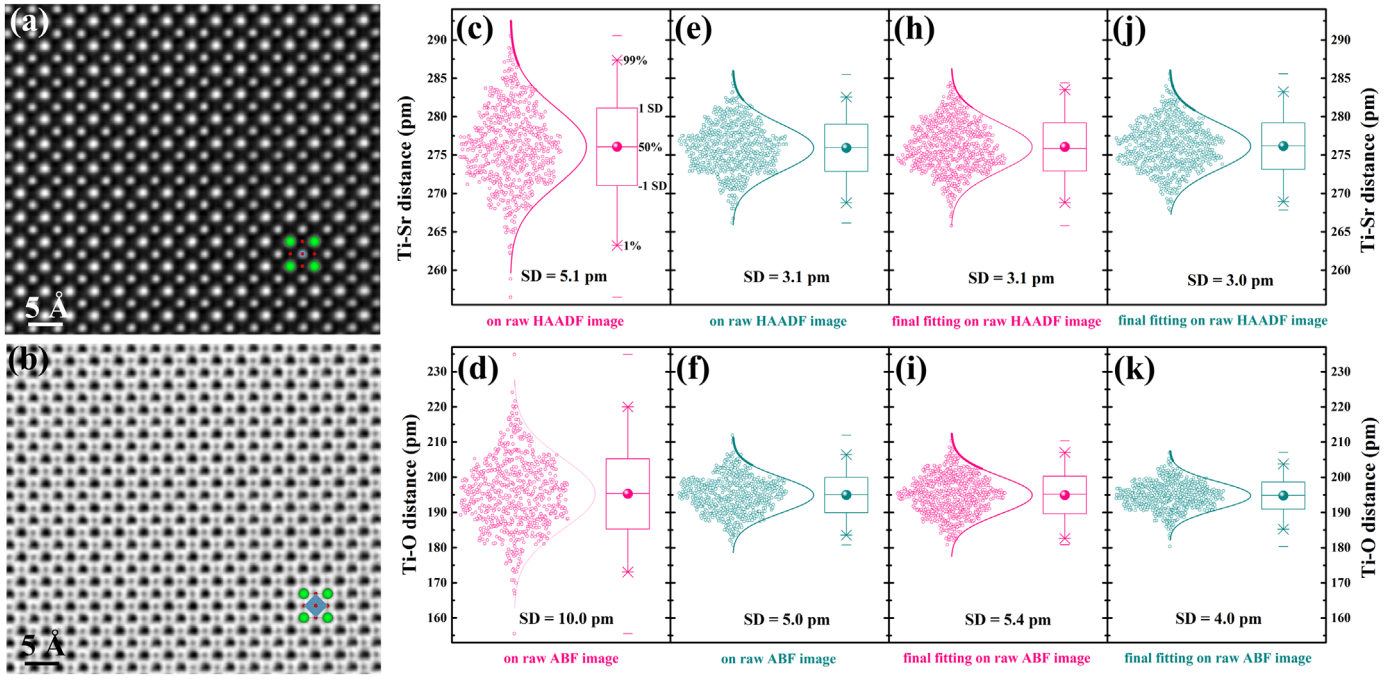

Fig. 3. Simultaneously acquired HAADF (a) and ABF (b) images of $SrTiO_3$ along the [100] zone axis. Raw frame serial images before and after alignment can be found in supplementary movies. (c) – (f) Box-and-whisker plot of the measured Ti–O and Ti–Sr atomic column distance for ABF and HAADF images, respectively. The pink color shows the results using center-of-mass method, and the turquoise color shows the results using 2D Gaussian fitting. The statistics are based on 168 TiO_6 octahedra (12 u.c. × 14 u.c.) measurements. In each plot, the left panel shows the raw data (the ordinate shows the measured distances, the width of scattering represents the relative frequency count) and a normal population curve; the right panel shows the summary of the statistics, the middle line in the box represents the median, the solid sphere is the mean, the box defines the standard deviation, and the whisker defines the 1%-99% range of the raw data. (For interpretation of the references to color in this figure legend, the reader is referred to the web version of this article.)

Supplementary material related to this article can be found online at http://dx.doi.org/10.1016/j.ultramic.2016.06.001.

5. Applications

To demonstrate the capability of the scripts, we show two examples.

5.1. Mapping oxygen octahedra in the ABO_3 structure

We demonstrate the use of the O–O picker tool for mapping the atomic column positions of a simulated STEM image of $SrRuO_3$, in which BO_6 octahedron rotation is present. The orthorhombic phase (Pnma, space group No. 62) with lattice parameters of $a=5.55$ Å, $b=7.84$ Å, and $c=5.56$ Å was used for STEM image simulation. Details of the crystallographic data can be found in Springer material phases data system [31]. The mapping of O atomic columns was performed on ABF images simulated along [101], [010], and [100] zone axes, as shown in Fig. 4. As illustrated by the superimposed atomic structure model in the figure, one can see that the shape of the projected RuO_6 octahedra is different in each orientation. The filled circles pinpoint the Ru (yellow) and O (red) atomic columns. In Fig. 4(a) and (b), the green lines connect the four oxygen atomic columns highlighting the frame of the projected RuO_6 octahedra. Because in [100] projection the apical-O atomic columns also contain Sr atoms, we map only the basal-plane O atomic columns. As can be seen from the pinpointed atomic positions, the O–O picker tool is able to successfully locate all the atomic positions in all these orientations. More quantitatively, as an example, we measure some typical values in each orientation, i.e, the oxygen to oxygen distance (d) in the [101] zone axis and the angle between basal directions of neighboring octahedra in [010] (θ_1) and [100] (θ_2) zone axis, as schematically shown at the bottom panel of each figure. The values measured from the simulated STEM images are $d_x=d_y=3.93\pm0.04$ Å, $\theta_1=167.14\pm0.57°$, and $\theta_2=161.34\pm0.76°$. These measured values are almost identical to the values ($d_x=d_y=3.93$ Å, $\theta_1=167.4°$, and $\theta_2=161.3°$) measured from the original atomic model.

5.2. A_2BO_4 structure mapping the oxygen octahedron deformation

Fig. 5 presents the atomically resolved HAADF (a) and ABF (b) images of the interface between $LaSrAlO_4$ and La_2CuO_4. The simulated HAADF and ABF images of the LSAO/LCO interface are superimposed on them, respectively, as highlighted by red rectangles. The lattice and BO_6 octahedral distortions were analyzed by the O–O picker scripts. Fig. 5(c) and (d) show the quantitative analyses of the structure distortion at the interface. Each data point was determined by averaging 10 unit cells of the perovskite lattice along the basal (vertical) direction, and the error bars give the 95% confidence interval (corresponding to 2 times the standard error of the average (mean)). It can be seen that in the basal direction both the La–La and O–O atomic column distances stay constant, indicating that the LCO film is under epitaxial compressive strain. However, the distance between Cu (Al) and the apical La atomic columns along the apical (growth) direction increases sharply at the interface and saturates in the LCO layer. This is also true for the apical oxygen–oxygen distance along the apical direction. This phenomenon is well known as biaxial strain in strain engineering, where the epitaxy layer is clamped to the substrate in the basal plane directions but free in the out-of-plane direction [32]. Another interesting phenomenon at the LSAO/LCO interface is that the relative change of the O–O distance is much stronger than that of the La(Cu)–La distance. This large Jahn–Teller distortion could originate from the apical oxygen having no hard contact with the nearest copper ion; it "levitates" on the electrostatic potential - a structural feature peculiar to certain layered oxides with alternating ionic planes of opposite charge [33]. This structural feature makes apical oxygen prone to very large displacements. A similar phenomenon has been observed by coherent Bragg rod analysis (COBRA) at the LSAO and Sr-doped LCO interface [34]. Another example of using this program for mapping lattice and CuO_6 octahedral distortion at the interfaces of two-dimensionally Sr-doped La_2CuO_4 can be found elsewhere [35].

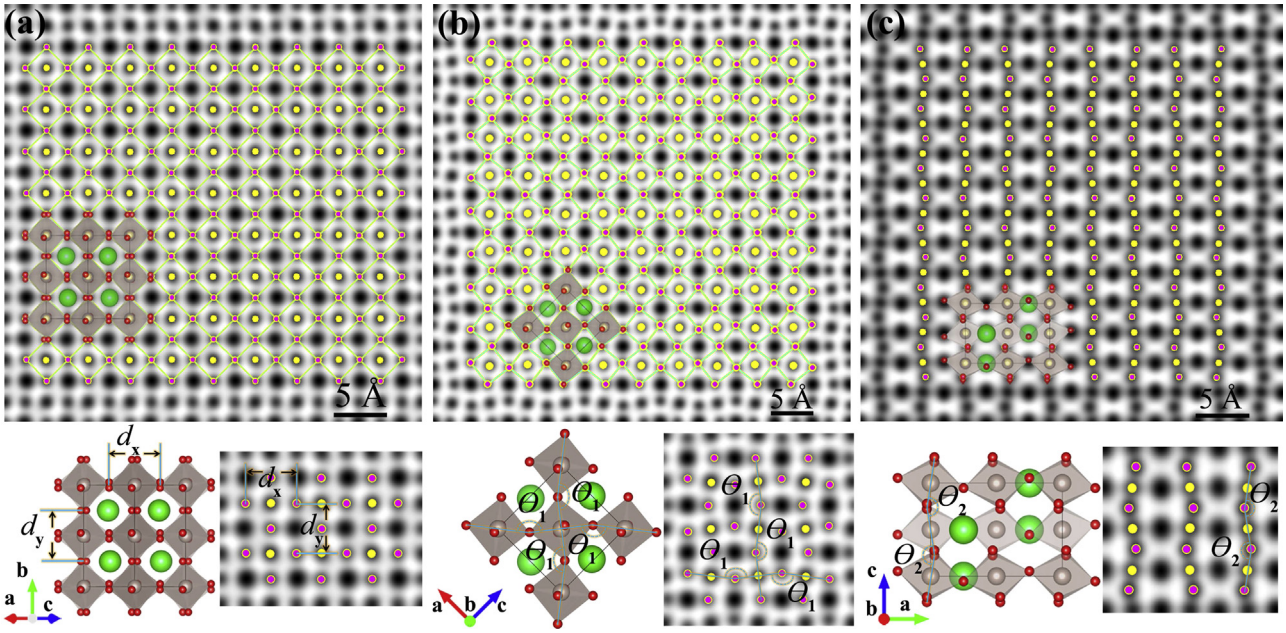

Fig. 4. Mapping of oxygen atomic columns and octahedral distortion in orthorhombic $SrRuO_3$. Simulated ABF images of $SrRuO_3$ along [101] (a), [010] (b), and [100] (c) zone axes. The atomic column positions pinpointed by the script are superimposed in the figure. The green lines in (a) and (b) highlight the shape of the projected RuO_6 octahedron. The definition of the measured distances and angles is presented in the bottom panel of each figure. (For interpretation of the references to color in this figure legend, the reader is referred to the web version of this article.)

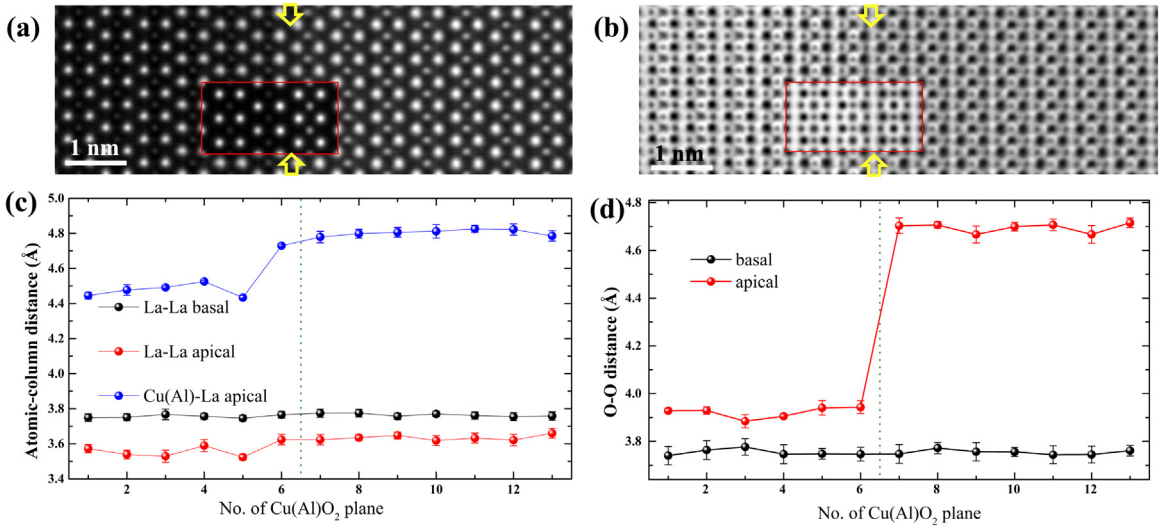

Fig. 5. Mapping BO_6 octahedral deformation at the $LaSrAlO_4/La_2CuO_4$ interface: (a) HAADF and (b) ABF images of the LSAO/LCO interface taken along the [100] crystallographic direction of LSAO. The insets show the simulated HAADF and ABF images of the LSAO/LCO interface (marked with a red rectangle). The yellow arrows on the image indicate the nominal position of the interface. (c) Quantitative analysis of basal and apical La–La atomic distances at the LSAO/LCO interface. (d) Quantitative analysis of the $Cu(Al)O_6$ octahedral deformation. (For interpretation of the references to color in this figure legend, the reader is referred to the web version of this article.)

6. Conclusion

A software tool for quantitative analysis of STEM images, i.e indexing the atomic column coordinates, extracting the lattice and the octahedral distortions, is introduced. In general, the results from both simulated and experimental STEM images (both HAADF and ABF) show that the 2D Gaussian fitting method gives better measurement precision than the center-of-mass method. We demonstrated that sub-picometer precision can be achieved on the simulated STEM images. Practically, under daily reproducible working conditions (sample drift and slight sample contamination present), we can achieve 3 picometer and 4 picometer measurement precisions for HAADF and ABF images, respectively. The program works well for different orientations of perovskite structures as well as for interfaces of oxide hetero-structures.

Acknowledgments

F. Baiutti, G. Gregori, G.Christiani, and G. Logvenov are gratefully acknowledged for providing the $La_2CuO_4/LaSrAlO_4$ heterostructure sample. The research leading to these results has received funding from the European Union Seventh Framework Program [FP/2007-2013] under grant agreement No. 312483 (ESTEEM2).

References

[1] R.H. Mitchell, Perovskites: Modern and Ancient, Almaz, Thunder Bay, Ontario, 2003.
[2] M. Haider, S. Uhlemann, E. Schwan, H. Rose, B. Kabius, K. Urban, Electron microscopy image enhanced, Nature 392 (1998) 768–769, http://dx.doi.org/10.1038/33823.
[3] S.D. Findlay, N. Shibata, H. Sawada, E. Okunishi, Y. Kondo, T. Yamamoto, Y. Ikuhara, Robust atomic resolution imaging of light elements using scanning transmission electron microscopy, Appl. Phys. Lett. 95 (2009) 191913, http://dx.doi.org/10.1063/1.3265946.
[4] S.D. Findlay, N. Shibata, H. Sawada, E. Okunishi, Y. Kondo, Y. Ikuhara, Dynamics of annular bright field imaging in scanning transmission electron microscopy, Ultramicroscopy 110 (2010) 903–923, http://dx.doi.org/10.1016/j.ultramic.2010.04.004.
[5] E. Okunishi, I. Ishikawa, H. Sawada, F. Hosokawa, M. Hori, Y. Kondo, Visualization of light elements at ultrahigh resolution by STEM annular bright field microscopy, Microsc. Microanal. 164 (2009) 15, http://dx.doi.org/10.1017/S1431927609093891.
[6] L. Gu, C.B. Zhu, H. Li, Y. Yu, C.L. Li, S. Tsukimoto, J. Maier, Y. Ikuhara, Direct observation of lithium staging in partially delithiated $LiFePO_4$ at atomic resolution, J. Am. Chem. Soc. 133 (2011) 4661–4663, http://dx.doi.org/10.1021/ja109412x.
[7] R. Ishikawa, E. Okunishi, H. Sawada, Y. Kondo, F. Hosokawa, E. Abe, Direct imaging of hydrogen-atom column in a crystal by annular bright-field electron microscopy, Nat. Mater. 10 (2011) 278–281, http://dx.doi.org/10.1038/nmat2957.
[8] C.T. Nelson, B. Winchester, Y. Zhang, S.-J. Kim, A. Melville, C. Adamo, C. M. Folkman, S.-H. Baek, C.-B. Eom, D.G. Schlom, L.-Q. Chen, X. Pan, Spontaneous vortex nanodomain arrays at ferroelectric heterointerfaces, Nano Lett. 11 (2011) 828–834, http://dx.doi.org/10.1021/nl1041808.
[9] G. Catalan, A. Lubk, A.H.G. Vlooswijk, E. Snoeck, C. Magen, A. Janssens, G. Rispens, G. Rijnders, D.H.A. Blank, B. Noheda, Flexoelectric rotation of polarization in ferroelectric thin films, Nat. Mater. 10 (2011) 963–967, http://dx.doi.org/10.1038/nmat3141.
[10] P.D. Robb, M. Finnie, A.J. Craven, Characterisation of InAs/GaAs short period superlattices using column ratio mapping in aberration-corrected scanning transmission electron microscopy, Micron 43 (2012) 1068–1072, http://dx.doi.org/10.1016/j.micron.2012.04.018.
[11] S. van Aert, J. Verbeeck, R. Erni, S. Bals, M. Luysberg, D. van Dyck, G. van Tendeloo, Quantitative atomic resolution mapping using high-angle annular dark field scanning transmission electron microscopy, Ultramicroscopy 109 (2009) 1236–1244, http://dx.doi.org/10.1016/j.ultramic.2009.05.010.
[12] J.M. LeBeau, S.D. Findlay, L.J. Allen, S. Stemmer, Standardless atom counting in scanning transmission electron microscopy, Nano Lett. 10 (2010) 4405–4408, http://dx.doi.org/10.1021/nl102025s.
[13] G.T. Martinez, A. Rosenauer, A. De Backer, J. Verbeeck, S. Van Aert, Quantitative composition determination at the atomic level using model-based high-angle annular dark field scanning transmission electron microscopy, Ultramicroscopy 137 (2014) 12–19, http://dx.doi.org/10.1016/j.ultramic.2013.11.001.
[14] A. Borisevich, H.J. Chang, M. Huijben, M.P. Oxley, S. Okamoto, M.K. Niranjan, J. D. Burton, E.Y. Tsymbal, Y.H. Chu, P. Yu, R. Ramesh, S.V. Kalinin, S.J. Pennycook, Suppression of octahedral tilts and associated changes in electronic properties at epitaxial oxide heterostructure interfaces, Phys. Rev. Lett. 105 (2010) 087204, http://dx.doi.org/10.1103/PhysRevLett.105.087204.
[15] A. Borisevich, O.S. Ovchinnikov, H.J. Chang, M.P. Oxley, P. Yu, J. Seidel, E. A. Eliseev, A.N. Morozovska, R. Ramesh, S.J. Pennycook, S.V. Kalinin, Mapping octahedral tilts and polarization across a domain wall in $BiFeO_3$ from Z-contrast scanning transmission electron microscopy image atomic column shape analysis, ACS Nano 4 (2010) 6071–6079, http://dx.doi.org/10.1021/nn1011539.
[16] J.-M. Zuo, A.B. Shah, H. Kim, Y. Meng, W. Gao, J.-L. Rouvière, Lattice and strain analysis of atomic resolution Z-contrast images based on template matching, Ultramicroscopy 136 (2014) 50–60, http://dx.doi.org/10.1016/j.ultramic.2013.07.018.
[17] S.M. Anthony, S. Granick, Image analysis with rapid and accurate two-dimensional Gaussian fitting, Langmuir 25 (2009) 8152–8160, http://dx.doi.org/10.1021/la900393v.
[18] Y. Feng, J. Goree, B. Liu, Accurate particle position measurement from images, Rev. Sci. Instrum. 78 (2007) 053704, http://dx.doi.org/10.1063/1.2735920.
[19] A.B. Yankovich, B. Berkels, W. Dahmen, P. Binev, S.I. Sanchez, S.A. Bradley, A. Li, I. Szlufarska, P.M. Voyles, Picometre-precision analysis of scanning transmission electron microscopy images of platinum nanocatalysts, Nat. Commun. 5 (2014) 4155, http://dx.doi.org/10.1038/ncomms5155.

[20] D.R.G. Mitchell, B. Schaffer, Scripting-customised microscopy tools for Digital Micrograph™, Ultramicroscopy 103 (2005) 319–332, http://dx.doi.org/10.1016/j.ultramic.2005.02.003.
[21] HREM Research - HREM Mouse Tool, ⟨http://www.hremresearch.com/Eng/plugin/plugin005/index.html⟩ (accessed 23.12.15).
[22] S. Van Aert, A.J. den Dekker, A. van den Bos, D. Van Dyck, High-resolution electron microscopy: From imaging towards measuring, IEEE Trans. Instrum. Meas. 51 (2002) 611–615, http://dx.doi.org/10.1109/TIM.2002.802250.
[23] F. Baiutti, G. Christiani, G. Logvenov, Towards precise defect control in layered oxide structures by using oxide molecular beam epitaxy, Beilstein J. Nanotechnol. 5 (2014) 596–602, http://dx.doi.org/10.3762/bjnano.5.70.
[24] M. Bosman, V.J. Keast, J.L. García-Muñoz, A.J. D'Alfonso, S.D. Findlay, L.J. Allen, Two-dimensional mapping of chemical information at atomic resolution, Phys. Rev. Lett. 99 (2007) 086102, http://dx.doi.org/10.1103/PhysRevLett.99.086102.
[25] C.T. Koch, Determination of Core Structure Periodicity and Point Defect Density Along Dislocations (Ph.D. thesis), Arizona State University, 2002, https://www.physik.hu-berlin.de/en/sem/images/koch02_phdthesis.pdf.
[26] R.C. Gonzalez, R.E. Woods, Digital Image Processing, 3rd ed., Prentice Hall, Upper Saddle River, NJ, 2007.
[27] S. Bals, S. van Aert, G. van Tendeloo, D. Ávila-Brande, Statistical estimation of atomic positions from exit wave reconstruction with a precision in the picometer range, Phys. Rev. Lett. 96 (2006) 096106, http://dx.doi.org/10.1103/PhysRevLett.96.096106.
[28] N. Mevenkamp, P. Binev, W. Dahmen, P.M. Voyles, A.B. Yankovich, B. Berkels, Poisson noise removal from high-resolution STEM images based on periodic block matching, Adv. Struct. Chem. Imaging 1 (2015) 3, http://dx.doi.org/10.1186/s40679-015-0004-8.
[29] L. Jones, P.D. Nellist, Identifiying and correcting scan noise and drift in scanning transmission electron microscopy, Microsc. Microanal. 19 (2013) 1050–1060, http://dx.doi.org/10.1017/S143192761300140 2.
[30] L. Jones, H. Yang, T.J. Pennycook, M.S.J. Marshall, S. Van Aert, N.D. Browning, M. R. Castell, P.D. Nellist, Smart align—a new tool for robust non-rigid registration of scanning microscope data, Adv. Struct. Chem. Imaging 1 (2015) 8, http://dx.doi.org/10.1186/s40679-015-0008-4.
[31] P. Villars, Material Phases Data System (MPDS), CH-6354 Vitznau, Switzerland (eds.) SpringerMaterials, $SrRuO_3-y$ ($SrRuO_3$ rt) Crystal Structure, Springer-Verlag GmbH, Heidelberg,© 2014. ⟨http://materials.springer.com/isp/crystallographic/docs/sd_1900510sd_1900510⟩.
[32] D.G. Schlom, L.-Q. Chen, C.J. Fennie, V. Gopalan, D.A. Muller, X. Pan, R. Ramesh, R. Uecker, Elastic strain engineering of ferroic oxides, MRS Bull. 39 (2014) 118–130, http://dx.doi.org/10.1557/mrs.2014.1.
[33] Z. Radović, N. Božović, I. Božović, Photoinduced expansion of cuprate superconductors: Evidence of strong electron-lattice coupling, Phys. Rev. B 77 (2008) 092508–092511, http://dx.doi.org/10.1103/PhysRevB.77.092508.
[34] H. Zhou, Y. Yacoby, V.Y. Butko, G. Logvenov, I. Božović, R. Pindak, Anomalous expansion of the copper-apical-oxygen distance in superconducting cuprate bilayers, Proc. Natl. Acad. Sci. USA 107 (2010) 8103–8107, http://dx.doi.org/10.1073/pnas.0914702107.
[35] Y. Wang, F. Baiutti, G. Gregori, G. Cristiani, U. Salzberger, G. Logvenov, J. Maier, P.A. van Aken, , Atomic-scale quantitative analysis of lattice distortions at interfaces of two-dimensionally Sr-doped La_2CuO_4 superlattices, ACS Appl. Mater. Interfaces 8 (2016) 6763–6769, http://dx.doi.org/10.1021/acsami.5b12813.